RSC Advances

PAPER

View Article Online
View Journal | View Issue

Cite this: *RSC Adv.*, 2017, **7**, 53097

TiO_2 hollow spheres on reduced graphene oxide with high rate performance as anodes for lithium-ion batteries†

Jicai Liang,[b] Xunlong Zhang,[a] Xiaojie Zhai,[a] Longjian Zhang,[c] Wenzheng Wu*[c] and Kaifeng Yu *[a]

Received 27th September 2017
Accepted 1st November 2017

DOI: 10.1039/c7ra10681e

rsc.li/rsc-advances

Anatase TiO_2 anchored on graphene oxide (GO) can be synthesized through a one-step hydrothermal method. The as-formed nanohybrid has a unique hollow structure and a large surface area. More importantly, compared to the pristine TiO_2 counterpart, TiO_2@RGO composite materials as anodes in lithium-ion batteries have demonstrated a uniform and highly crystallized morphology and exhibited excellent cycling stability and rate capability of 352 mA h g^{-1} at 0.5C and 223 mA h g^{-1} at 5C after 100 cycles, indicating that the TiO_2@RGO nanocomposite has promise in advanced Li-ion batteries. The improvement of electrochemical performance is assigned to the enhanced conductivity in the presence of GO in the TiO_2@RGO nanocomposite, the anatase and TiO_2–B mixed crystal phase of the hollow sphere TiO_2@RGO nanocomposite, the small size of TiO_2 particles in the nanocomposite, and the enlarged electrode/electrolyte contact area, leading to more active sites in TiO_2@RGO.

Introduction

Lithium ion batteries (LIBs) have gained growing interest because of their wide applications in portable electronic devices as well as electronic vehicles due to their high capacity, long cycle life and environmental benignity.[1–3] Particularly, titanium dioxide (TiO_2), has been attracting much attention because of its low price, non-toxicity and low volume expansion (<4%) during the Li-ion insertion–extraction processes.[4–6] In addition, owing to the higher Li-ion intercalation potential (1.5–1.8 V *versus* Li^+/Li) of TiO_2, the generation of lithium dendrites could be suppressed. Its reaction process can be described properly with the following equation: $TiO_2 + xLi^+ + xe^- \rightarrow 2Li_xTiO_2$ ($0 \leq x \leq 0.5$). However, the theoretical capacity of anatase and rutile phase TiO_2 is only 168 mA h g^{-1}.[7–9] Meanwhile, the reunion and decomposition of TiO_2 during charge–discharge cycles can result in the reduction of active sites and the degradation of specific capacity, which definitely hinder the application of TiO_2 in LIB anode materials.[10] In order to improve electrical and ionic conductivities, adding some conductive materials, for example, carbon nanomaterials, metals, metal oxides and polymers, is a common practice. In this way, we can shorten the transmission distance and decrease the resistance of intrinsic electrons and lithium ions. At same time, different structures of TiO_2, such as 1D nanowires or nanotubes, 2D nanosheets and even complicated 3D structures, can get higher capacities and high rate capabilities in the electrodes of lithium ions batteries based on following reason: higher surface area which is beneficial to increase the contact area between electrolyte and electrode, resulting in an excellent cycling performance of electrode materials.

Compared with conventional conductive additives, graphene, with a ultrathin two-dimensional carbon sheet, has lots of unique properties, for example, high electronic conductivity, large specific surface area and high structural flexibility.[11–13] Due to the TiO_2 loading on the graphene showed excellent electrochemical performance such as high rate capacity, shortened transport length of electrons, and enhanced contact area of electrolyte–electrode, TiO_2/GO nanocomposites have been achieving a wide attention for exploring Li storage based on above advantages.[14–16] Li *et al.* adopted the hydrothermal method to fabricate mesoporous anatase TiO_2 nanospheres anchoring onto graphene sheets, which demonstrated a reversible capacity of 200 mA h g^{-1} at the rate of 1C after 100 cycles.[17] Zhen *et al.* used hydrothermal process to construct mesoporous structure TiO_2/RGO hybrid materials, which possessed an excellent capacity retention about 260 mA h g^{-1} at 1.2C after 400 cycles.[18] However, most of their experimental process are quiet complex and are not easily operated in the practical application. Therefore, exploring a simple, facile and easy-to-handle method to synthesize well-dispersed TiO_2/GO hybrid anode materials

[a]*Key Laboratory of Automobile Materials, Ministry of Education, College of Materials Science and Engineering, Jilin University, Changchun 130025, China. E-mail: yukf@jlu.edu.cn*

[b]*Roll Forging Institute of Jilin University, Changchun 130022, China*

[c]*School of Mechanical Science and Engineering, Jilin University, China. E-mail: wzwu@jlu.edu.cn*

† Electronic supplementary information (ESI) available. See DOI: 10.1039/c7ra10681e

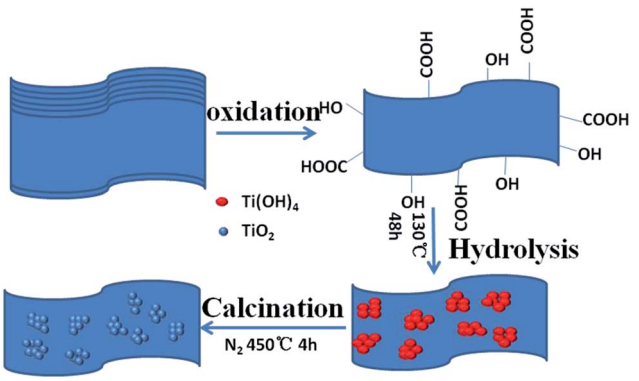

Scheme 1 Scheme of the synthesis TiO_2@RGO nanocomposite.

which possessed properties of structural stability and great performance is particularly important.

In this paper, we propose a simple strategy to fabricate nanostructured hollow spheres TiO_2@RGO anode materials which make nanocrystalline TiO_2 grown *in situ* on graphene *via* a facile template-free one-step followed by calcinations.

Compared with the reported hydrothermal–solvothermal routes, the current experiment schemes were performed without addition of any surfactants. It only use tetrabutyl titanate($Ti(OR)_4$), LiOH and GO as the raw materials. What is novel about our work is that there are few literatures on the synthesizing nanostructured hollow spheres TiO_2@RGO electrode used TBT as precursor *via* template-free one-step *in situ* method which was deployed in LIBs. It delivers the characteristics of hollow structures with large surface area and highly mesoporous structures. We significantly improve the electrochemical performance of anode materials and preparation procedures of TiO_2@RGO composite materials. As a result, the excellent electrochemical performance of as-prepared TiO_2@RGO electrode materials shows its great potential values in advanced Li-ion batteries under a high-rate current density. Scheme 1 illustrates the synthesis process of the TiO_2@RGO nanocomposite.

Experiment

Preparation of GO

Graphene oxide was prepared *via* the oxidation of graphene by applying improved Hummers' method.[44]

Preparation of nanostructure TiO_2@RGOcomposites

In a typical synthetic procedure, 50 mg GO was dissolved in 30 mL solution containing 5.0 g LiOH, followed by ultrasound for 2 h. Then, 2 mL tetrabutyl titanate (TBT) was dispersed into the above solution drop by drop along with vigorous agitation for 30 min and ultrasounded for another two hours. Thereafter, the mixture was placed into a 50 mL Teflon-lined autoclave and maintained at 130 °C for 48 h. After naturally cooled to room temperature, the obtained products were soaked in 0.1 M H_2SO_4 solution for some time, centrifuged and washed several times by distilled water and ethanol until the pH value was close to 7, then dried at 60 °C in oven for 24 h and annealed at 450 °C for 4 h under nitrogen to get the final product, namely, the TiO_2-reduced graphene oxide (termed as TiO_2@RGO) nanocomposite. The fabrication of the pure TiO_2 nanoparticles, a similar process was proceeded without the addition of GO in the original solution.

Material characterizations

The X-ray diffraction (XRD) patterns were carried out on a Bruker D8 Advance X-ray Diffractometer. Raman spectroscopy (Renishaw, 633 nm excitation) was used to characterize the interaction among of TiO_2 and GO. Structure and morphology of TiO_2@RGO-Nd nanohybrid, the TiO_2@RGO and the pure TiO_2 were observed by a transmission electron microscope (TEM; JSM-2100F) and a Cold Field Scanning electron microscope (SEM; JSM-7500F). Nitrogen adsorption/desorption tests were conducted at Brunauer–Emmett–Teller (BET) measurements (JW-BK222 surface area analyzer).

Electrochemical measurements

The electrochemical measurements were carried out with two-electrode CR2025 coin cells. The working electrode was prepared by mixing 80 wt% active material (TiO_2@RGO), 10 wt% carbon black and 10 wt% polyvinylidene fluoride (PVDF). Then the mixture was dissolved in *N*-methyl-2-pyrrolidone under stirring. The slurry was coated onto a Cu foil and dried at 120 °C for 12 h. The loading mass of active material was approximately 0.43 mg cm^{-2}. The electrochemical measurements were carried out with two-electrode CR2025 coin cells. The lithium foil was used as the counter and reference electrodes, Celgard 2300 as the separator and 1 M $LiPF_6$ as the electrolyte. Constant current charge–discharge tests were carried out on a Land Battery Measurement System (CT2001A) at various current densities with a cut off voltage of 1–2.5 V at room temperature. Cyclic voltammograms (CV) at a scan rate of 0.2 mV s^{-1} and electrochemical impedance spectra over a frequency range of 100 kHz to 0.1 Hz were measured on a CHI660E electrochemical work station at room temperature.

Results and discussion

Morphology and structural characterization

The crystallographic structure of the samples can be provided by X-ray diffraction (XRD) patterns. As shown in Fig. 1a, the pure

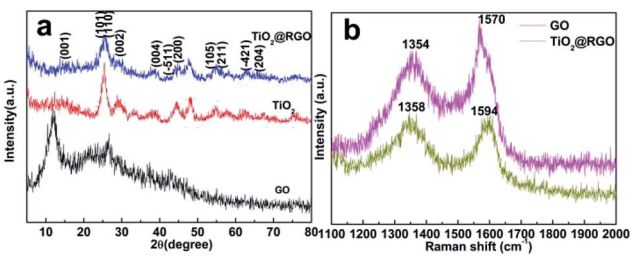

Fig. 1 (a) XRD patterns of TiO_2@RGO, TiO_2 and (b) Raman spectra of TiO_2@RGO and RGO.

TiO_2 exhibits good crystallinity. The peaks at 25.3°, 37.8°, 48.1°, 55.1° and 62.8° correspond to the lattice planes of (101), (004), (200), (211), (204), respectively,[19] indicating that the TiO_2 is anatase phase (JCPDS no. 21-1272).[20,21] At the same time, the XRD patterns of the TiO_2@RGO nanocomposite retain the same position of the diffraction peaks.

However, the diffraction peaks of the TiO_2 in the TiO_2@RGO nanocomposite become broader and lower, demonstrating a small crystallite size. Meanwhile, the XRD spectrums of hybrid nanocomposite and pure TiO_2 all display a typical TiO_2–B diffraction peaks (space group $C2/m$, JCPD no. 35-0088) at 14.3°, 25.0°, 28.7°, 44.7° and 58.4° corresponding to the (001), (110), (002), (−511), (−421) reflections, respectively.[22] The skeleton of the TiO_2–B structure is consisted of corrugated sheets of edge and corner-sharing TiO_6 octahedra that are linked by bridging oxygen atoms, formed a three-dimensional network. This nanostructure is more open than those of rutile and anatase, which makes the material an effective host for lithium ions storage.[23,24] One diffraction peak centered at $2\theta = 11.41°$ corresponds to the (001) reflection of GO with an interlayer spacing of 7.75 Å.[25] The peak disappeared in the following compound process, indicating that the GO nanosheets have been completely reduced to RGO nanosheets using the current hydrothermal treatment. In the same position, the TiO_2@RGO nanocomposite don't have the characteristic peaks of GO, showing that the TiO_2 uniformly dispersed on the GO nanosheets. Fig. 1b shows the Raman spectra of GO before and after deposition of TiO_2. The GO exhibited Raman shifts at approximately 1354 and 1570 cm^{-1} corresponding to the D and G bands, respectively. After heat-treatment at 450 °C, the D and G bands of TiO_2@RGO located at about 1358 and 1594 cm^{-1}. The intensity of D band to G band (I_D/I_G) for the TiO_2@RGO (1.06) is a bit higher than that of GO (0.85). The intensity of D band to G band (I_D/I_G) for the TiO_2@RGO (1.06) is a bit higher than that of GO (0.85), indicating the reduction of GO in the TiO_2@RGO nanocomposite.

When TBT was added into GO sheets, the TiO_2 nanoparticles homogeneously anchored on RGO nanosheets. The morphology of TiO_2@RGO hybrid electrode material, GO and pure TiO_2 were observed *via* scanning electron microscopy (SEM). It can be clearly seen that GO has a wrinkled flake-like structure in Fig. 2a and b, which is in accorded with the results in the recent article.[45,46] As shown in the Fig. 3a and c, the TiO_2 were regularly spherical. Fig. 3c shows that the TiO_2 nanospheres are well-dispersed and uniformly attached on the surface of the RGO nanosheets. The TiO_2 exhibited good dispersibility in the pure phase and composite electrode materials. To further explore the microstructure of the materials, the products were investigated by transmission electron microscopy (TEM). It can be seen that the TiO_2 exhibits a hollow sphere structure with uniform particle size in Fig. 3b. The hollow structure of the TiO_2 nanocomposite remained unchanged as shown in Fig. 3d. There is no structure collapse before and after the composite. The hollow structure can be seen clearly in Fig. 3b and d. The wall thickness of TiO_2 hollow nanostructures is about 2–4 nm. The TiO_2 possesses nearly spherical structure with the size of particle about 10 nm and deliver good features, such as more

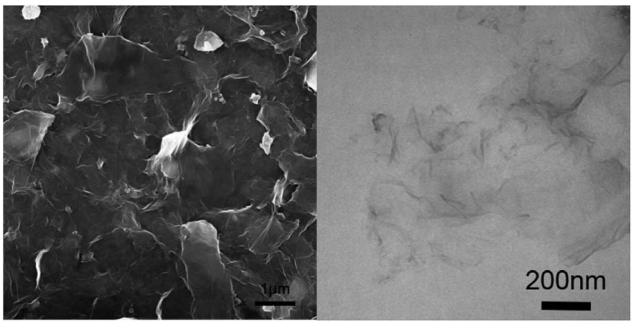

Fig. 2 SEM and TEM images of bare GO.

stable, active site distribution more uniform, high specific surface area, wall thickness in 2–4 nm, which are contribute to the ions and electrons transfer, beneficial to the improvement of the capacity. The combination of TiO_2 materials with such structure advantages and graphene materials will greatly increase the performance of TiO_2 as anode material. The selected area electronic diffraction nanostructure pattern (SAED) of the hollow spheres TiO_2@RGO nanostructure delivers a set of diffraction rings of the anatase and TiO_2–B structure of the TiO_2, indicating the polycrystalline nature of the products, which can be clearly assigned to the anatase TiO_2 and TiO_2–B, respectively. This result is consistent with the XRD results. As shown in Fig. 3d, the TiO_2@RGO composites, in which the hollow spheres were uniformly and well dispersedly attached on the surface of RGO sheets. Fig. 3e is the High-Resolution TEM(HRTEM) image of TiO_2@RGO. As shown in Fig. 3e, the

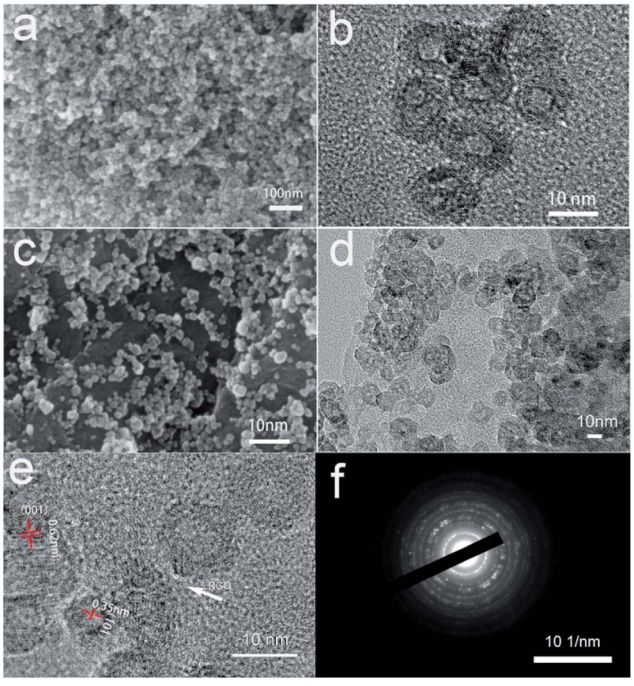

Fig. 3 SEM (a) and TEM (b) images of pure TiO_2, SEM (c) and TEM (d) images of TiO_2@RGO nanocomposite, HRTEM (e) and SAED (f) images of TiO_2@RGO.

lattice fringes with the spaces of 0.35 nm and 0.62 nm correspond to the (101) and (001) of anatase TiO_2 and TiO_2–B, respectively. Elemental mapping and EDX spectrum for TiO_2@RGO nanocomposite are also shown in Fig. S1 (in the ESI†). The corresponding element mapping images (Fig. S1†) of C, Ti, and O in the TiO_2@RGO nanocomposite overlapped with each other, indicating the uniform distribution of these elements and the nanohollow sphere TiO_2 are evenly distributed across the surfaces of rGO. The corresponding EDX of the selected area is also depicted in Fig. S1e,† which agrees well with the mapping results, except for the Si peaks that originated from silicon substrate. Based on the EDS elements mapping analysis, we confirm that it has a unique hollow structure.

Nitrogen isotherm adsorption–desorption curves with the pore size distributions of the pristine TiO_2 and TiO_2@RGO are presented in Fig. 4a and b. For TiO_2@RGO, a type IV isotherm is observed, which is characteristic of mesoporous materials.[49] Based on the Barrett–Joyner–Halenda (BJH) equation, the main pore size (inset in Fig. 4b) in TiO_2@RGO is 8.5 nm less than 11.6 nm of the pure TiO_2(inset in Fig. 4a). It is in agreement with the pore size determined from the TEM images and the results described in the XRD, which further confirms a uniform pore size distribution. Compared to the specific surface area (105.5 $m^2\ g^{-1}$) of the TiO_2, the specific surface area of TiO_2@RGO is 145.8 $m^2\ g^{-1}$. The larger surface area of TiO_2@RGO is conductive to increasing contact area of electrode–electrolyte and can improve diffusion of electrolyte ions.

The electrochemical performance of the prepared pure TiO_2 and TiO_2@RGO materials were investigated as electrode for LIBs. Fig. 5a and b shows the discharge–charge curves of the pure TiO_2 and TiO_2@RGO at a rate of 0.5C (1C = 168 mA h g^{-1}) in the potential window of 1.0–2.5 V *versus* Li^+/Li in the 1st, 2nd, 10th, 50th and 100th. The initial discharge–charge capacities of the pure TiO_2 were 570/399 mA h g^{-1}, and subsequently deceased to just 223 mA h g^{-1} after 100 cycles. As a comparison, the TiO_2@RGO hybrid nanocomposite obtained higher capacities with 634/388 mA h g^{-1} at the first cycle. The columbic efficiency of the pure TiO_2 and TiO_2@RGO is comparatively low in the first cycle, which can be attributed to the existence of irreversible Li trapped sites.[26] There are two obvious plateaus at 1.75 V and 1.95 V, corresponding to Li^+ insertion and Li^+ extraction between the TiO_2 nanoparticles and $Li_{0.5}TiO_2$, which meet the characteristics of anatase TiO_2 lithiation.[47,48]

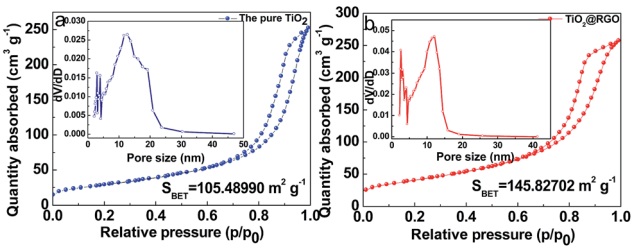

Fig. 4 Nitrogen isotherm adsorption–desorption curves of (a) the pure TiO_2 and (b) TiO_2@RGO. The inset in (a) and (b) show pore-size distributions of the pure TiO_2 and TiO_2@RGO.

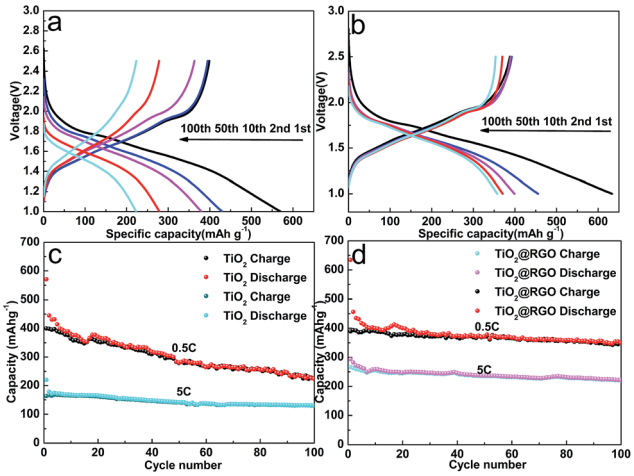

Fig. 5 Discharge–charge profiles of (a) pure TiO_2 and (b) TiO_2@RGO; cycling performance of (c) pure TiO_2 and (d) TiO_2@RGO at 0.5C and 5C.

Meanwhile, it is obvious to see that there are huge differences of plateau voltage between pure TiO_2 and TiO_2@RGO hybrid electrode, indicating that the TiO_2@RGO nanocomposites possessed excellent reaction kinetics and low polarization. Compared with TiO_2@RGO electrode, the redox potential plateaus of pure TiO_2 is getting smaller and smaller until it disappeared in the end because of its bigger size and inherently bad electronic conductivity. Fig. 5c and d depicts the cycling performance of the pristine TiO_2 and TiO_2@RGO electrode at a rate of 0.5C and 5C. Just as showed in Fig. 5d, the TiO_2@RGO hybrid composite displays excellent reversible capacity and cycle characteristics. The results demonstrated that the TiO_2@RGO electrode obtained high reversible capacity of 352 mA h g^{-1} (0.5C) and 223 mA h g^{-1} (5C) up to 100 cycles, which were higher than that of anode materials composed of anatase TiO_2 nanospheres/hollow structures, rutile TiO_2 nanorods/porous microspheres/nanoparticles, *etc.*[27–32] At the same time, the initial discharge–charge capacities of pure anatase TiO_2 were 570/399 mA h g^{-1}, which demonstrate that the pure phase TiO_2 has high specific capacity. The first discharge capacity of TiO_2 is about 570 mA h g^{-1}, a value much higher than the theoretical capacity of TiO_2. It can be explained that the specific surface area of pure TiO_2 is 105.5 $m^2\ g^{-1}$ and the specific surface area of TiO_2@rGO is more than 145.8 $m^2\ g^{-1}$. The large specific surface area plays an important role in the consumption of lithium ion at initial discharge process. At the same time, the formation of the SEI film will consume a large amount of lithium ion. The reasons for the above statement will lead to the increase of capacity. Subsequently, discharge capacities of pure anatase TiO_2 quickly decreased to 129 mA h g^{-1} at 5C and about 223 mA h g^{-1} at 0.5C (after 100 cycles) accompanied by capacities rose and downed which could be attributed to the activation and the structure collapsed of active materials.[33] Meanwhile, on the other hand, we can see that the pure TiO_2 electrode has the potential value based on its high initial capacities. Compared with pure TiO_2 electrode, TiO_2@RGO shown a higher rate performance and ultra long

cycle life for lithium storage, which could be attributed to its unique hollow nanostructure, relatively large surface areas (the particle size of sample is about 8.5 nm). Also, RGO nanosheets can benefit to restraining grain growth and inhabit anatase TiO_2 aggregation. Fig. 6 shows the rate performance of the pure TiO_2 and TiO_2@RGO hybrid composites at different rates. When cycled at the rate of 0.5, 1, 2 and 5C, the reversible discharge capacities of the pure TiO_2 were 263, 229, 198, and 147 mA h g^{-1}, respectively. Compared with pure TiO_2 electrode, the TiO_2@RGO hybrid composites owned higher reversible capacities of 585, 509, 434, 354 mA h g^{-1}, respectively. Especially, there are no obvious capacity recession when the rate returned to 2, 1 and 0.5C, which demonstrated that TiO_2@RGO hybrid composites possess excellent electrochemical properties even at high rates due to the superiority of taken experimental methods and unique features of hybrid nanostructure. The performance of TiO_2@RGO hybrid composites were superior to other the report results.[34,35] As a typical example, Lee *et al.* fabricated TiO_2 nanorod arrays on RGO as LIB anodes, and the capacity was only 94 mA h g^{-1} at 5C less than the capacity of 354 mA h g^{-1} at 5C in this article.[36] In order to verify the characteristics of the synthesized electrode materials, the electrochemical performance of the nanohybrid was analyzed by the charge/discharge cycle at a high rate. As shown in Fig. 6b, the charge–discharge curve was well fitted and the capacity remained at 217 mA h g^{-1} at a rate of 10C after 2000 cycles, indicating a good capacity retention, high specific capacity, good cycle reversibility and stability of the material.

In order to further explore the synergistic effects of RGO nanosheets and the pristine TiO_2, the CV curve was tested for the first three cycles of the Li-ion half-cell at a voltage range of 1–2.5 V *vs.* Li/Li^+ at a scanning speed of 0.1 mV s^{-1}. As shown in the figure, hybrid TiO_2@RGO spectrums have three pairs of obvious oxidation (insertion) and deoxidization (extraction) peaks, with the first red-ox peaks of 1.49/1.54, 1.57/1.68 and 1.73/1.98 V, respectively. The second and third cycles of red-ox peaks correspond to 1.49/1.54, 1.57/1.68, 1.73/1.98 V. The red-ox peaks appearing on the first cycle are shifted relative to the second and third cycle, which is due to the initial decomposition of the electrolyte in the hybrid electrode and the formation of the mesophase of the solid electrolyte interphase (SEI).[37,38] The pair of cathodic/anodic peaks at 1.73/1.98 V correspond to the anatase TiO_2 electrode. The relatively weak peaks at 1.49/1.54 and 1.57/1.68 V correspond to the red-ox peaks for Li/Li^+ embedded/out in the TiO_2–B, indicating the content of Li/Li^+ is relatively less than that of anatase TiO_2. It agrees with the results of XRD analysis. The CV curve of the first cycle and the next two cycles CV spectrums suggest the first irreversible charge–discharge capacity of hybrid electrode and lost capacity (Fig. 7). The second and third CV curves are well overlapped, which indicate that the hybrid electrode has excellent cycle performance, high reversibility and good capacity retention.

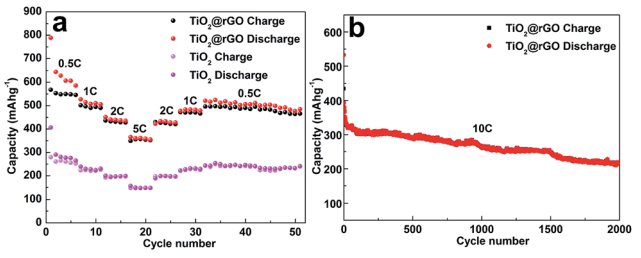

Fig. 6 (a) Rate performance of TiO_2@RGO nanocomposite and pure TiO_2 at various current densities between 0.5C and 5C. (b) Durability test at high 5C and 10C currents of the TiO_2@RGO at 5C and 10C.

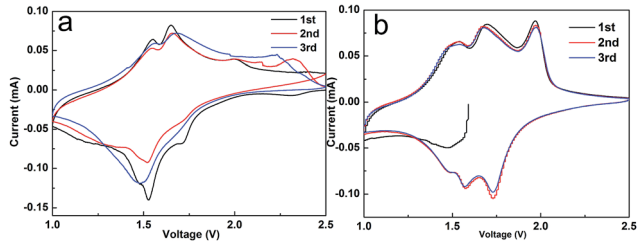

Fig. 7 CV curve of (a) pure TiO_2 and (b) TiO_2@RGO nanocomposite.

To gain insight into the remarkable rate performance of the TiO_2@RGO composites, electrochemical impedance spectroscopy (EIS) was performed on the cells consisting of pure TiO_2 and TiO_2@RGO composites as the working electrode *vs.* Li without discharge and charge cycles before cycles. Fig. 8, the Nyquist plots display an inclined line in the low-frequency range and only one semicircle in the high-frequency range. The inclining line and high frequency oblate semicircle correspond to the Li^+ diffusion process and charge-transfer impedance in the electrode/electrolyte interface, respectively.[39] Compared with pure TiO_2 (132 Ω), TiO_2@RGO nanostructure has a smaller resistance value of 69.2 Ω that can effectively improve the electron transport.

The enhanced lithium storage performance could be assigned to the following reasons. On the one hand, the fabrication of the anatase TiO_2 itself has a unique hollow crystal nanostructure that facilitate the Li ion diffusion owing to the

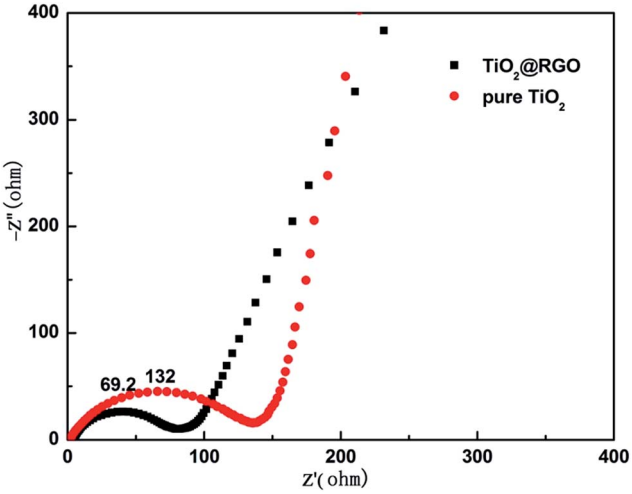

Fig. 8 Nyquist plots for the EIS of TiO_2@RGO and pure TiO_2 electrodes before cycling.

open channels and the shortened transport pathways, a small grain size (less than 10 nm) and a large surface that which benefits to the contact area between the electrode and the electrolyte. On the other hand, the functional active groups on the surface of RGO nanosheets, such as –OH, –COOH, are conductive to adhesion of the hollow anatase TiO_2 which can reduce the aggregation of TiO_2 and make the TiO_2 obtain a good dispersibility. At the same time, it benefits the combination of RGO nanosheets and the hollow anatase TiO_2 that can achieve a more stable hybrid nanostructure composite. The aggregation of TiO_2 and stacking of GO can be effectively prevented, leading to good cycling performance. Last but not least, the conductivity of RGO nanosheets with large surface and the layered structure is an effective tool for solving the poor electrical conductivity of pure TiO_2, enhancing the quality of the electrode–electrolyte contact, providing abundant nanoporous channels for Li^+/electron transfer and preventing the aggregation of anatase TiO_2.[40–43] The synergistic effect of nanostructured TiO_2 and RGO is a main factor for the superior rate capability and excellent cycle ability of the TiO_2@RGO nanohybrid.

Conclusions

We have developed a facile *in situ* hydrothermal synthesis approach to construct a hollow TiO_2@RGO nanohybrid composite. The combination of the TiO_2 has an open crystal structure, a small particle size and a large surface. Compared with the pristine TiO_2 and other TiO_2@RGO nanocomposites prepared through hydrothermal/solvothermal approaches, the as-prepared TiO_2@RGO nanocomposite shown significantly enhanced lithium storage performance, much higher reversible capacity, and better cycling stability. More importantly, the as-prepared TiO_2@RGO nanocomposite still showed a higher reversible capacity for 220 mA h g^{-1} at 5C current after 100 cycles. The simple and steerable synthesis, excellent electrochemical performance, and the hollow sphere structure could also provide a new idea for developing higher-performance lithium storage electrodes and other energy storage applications.

Conflicts of interest

There are no conflicts to declare.

Acknowledgements

This work was financially supported by National Science Foundation of China (51275203).

Notes and references

1 P. Meduri, E. Clark, J. H. Kim, E. Dayalan, G. U. Sumanasekera and M. K. Sunkara, *Nano Lett.*, 2012, **12**, 1784–1788.
2 B. Scrosati, *Nature*, 1995, **373**, 557–558.
3 M. Ling, J. X. Qiu, S. Li, H. Zhao, G. Liu and S. Q. Zhang, *J. Mater. Chem. A*, 2013, **1**, 11543–11547.
4 Z. C. Yan and L. Liu, *Electrochim. Acta*, 2014, **123**, 551–559.
5 A. G. Dylla, G. Henkelman and K. J. Stevenson, *Acc. Chem. Res.*, 2013, **46**, 1104–1112.
6 J. Xu, C. H. Jia, B. Cao and W. F. Zhang, *Electrochim. Acta*, 2007, **52**, 8044–8047.
7 M. Zukalová, M. Kalbáč, L. Kavan, I. Exnar and M. Graetzel, *Chem. Mater.*, 2005, **17**, 1248–1255.
8 X. B. Wang, Y. Yan, B. Hao and G. Chen, *ACS Appl. Mater. Interfaces*, 2013, **5**, 3631–3637.
9 L. F. He, R. G. Ma, N. Du, J. G. Ren, T. L. Wong, Y. Y. Li and S. T. Lee, *J. Mater. Chem.*, 2012, **22**, 19061–19066.
10 H. Kim, M. Kim, T. Shin, H. Shin and J. Cho, *Electrochem. Commun.*, 2008, **10**, 1669–1672.
11 T. B. Lan, Y. B. Liu, J. Dou, Z. S. Hong and M. D. Wei, *J. Mater. Chem. A*, 2014, **2**, 1102–1106.
12 R. W. Mo, Z. Y. Lei, K. N. Sun and D. Rooney, *Adv. Mater.*, 2014, **26**, 2084–2088.
13 W. Li, F. Wang, S. S. Feng, J. X. Wang, Z. K. Sun, B. Li, Y. H. Li, J. P. Yang, A. A. Elzatahry, Y. Y. Xia and D. Y. Zhao, *J. Am. Chem. Soc.*, 2013, **135**, 18300–18303.
14 F. Zhang, H. Q. Cao, D. M. Yue, J. X. Zhang and M. Z. Qu, *Inorg. Chem.*, 2012, **51**, 9544–9551.
15 G. P. Xiong, K. P. S. S. Hembram, R. G. Reifenberger and T. S. Fisher, *J. Power Sources*, 2013, **227**, 254–259.
16 G. P. Xiong, C. Z. Meng, R. G. Reifenberger, P. P. Irazoqui and T. S. Fisher, *Adv. Energy Mater.*, 2014, **4**, 1300515.
17 N. Li, G. Liu, C. Zhen, F. Li, L. L. Zhang and H. M. Cheng, *Adv. Funct. Mater.*, 2011, **21**, 1717–1722.
18 M. Zhen, X. Guo, G. Gao, *et al.*, *Chem. Commun.*, 2014, **50**(80), 11915–11918.
19 P. D. Cozzoli, A. Kornowski and H. Weller, *J. Am. Chem. Soc.*, 2003, **125**, 14539–14548.
20 H. B. Wu, X. W. Lou and H. H. Hng, *Chem.–Eur. J.*, 2012, **18**, 2094–2099.
21 J. H. Liu, J. S. Chen, X. F. Wei, X. W. Lou and X. W. Liu, *Adv. Mater.*, 2011, **23**, 998–1002.
22 C. J. Chen, X. L. Hu, Z. H. Wang, X. Q. Xiong, P. Hu, Y. Liu and Y. H. Huang, *Carbon*, 2014, **69**, 302–310.
23 R. Marchand, L. Brohan and M. Tournoux, *Mater. Res. Bull.*, 1980, **15**, 1129–1133.
24 Y. D. Yin, R. M. Rioux, C. K. Erdonmez, S. Hughes, G. A. Somorjai and A. P. Alivisatos, *Science*, 2004, **304**, 711–714.
25 J. Zhang, H. Yang, G. Shen, P. Cheng, J. Zhang and S. Guo, *Chem. Commun.*, 2010, **46**, 1112–1114.
26 C. Lai, H. Z. Zhang, G. R. Li and X. P. Gao, *J. Power Sources*, 2011, **196**, 4735–4740.
27 Y. Wang, X. W. Su and S. Lu, *J. Mater. Chem.*, 2012, **22**, 1969–1976.
28 H. Qiao, Y. W. Wang, L. F. Xiao and L. Z. Zhang, *Electrochem. Commun.*, 2008, **10**, 1280–1283.
29 H. Kaper, F. Endres, I. Djerdj, M. Antonietti, B. M. Smarsly, J. Maier and Y. S. Hu, *Small*, 2007, **10**, 1753–1763.
30 E. Baudrin, S. Cassaignon, M. Koelsch, J. P. Jolivet, L. Dupont and J. M. Tarascon, *Electrochem. Commun.*, 2007, **9**, 337–342.

31 H. E. Wang, H. Cheng, C. P. Liu, X. Chen, Q. L. Jiang, Z. G. Lu, Y. Y. Li, C. Y. Chung, W. J. Zhang, J. A. Zapien, L. Martinu and I. Bello, *J. Power Sources*, 2011, **196**, 6394–6399.
32 M. C. Yang, Y. Y. Lee, B. Xu, K. Powers and Y. S. Meng, *J. Power Sources*, 2012, **207**, 166–172.
33 G. X. Hu, X. Cai and Y. H. Rong, *Fundamentals of Materials Science*, Shanghai Jiao Tong University Press, Shanghai, 1st edn, 2000.
34 H. Cao, B. Li, J. Zhang, F. Lian, X. Kong and M. Qu, *J. Mater. Chem.*, 2012, **22**, 9759–9766.
35 R. Giannuzzi, M. Manca, L. D. Marco, M. R. Belviso, A. Cannavale, T. Sibillano, C. Giannini, P. D. Cozzoli and G. Gigli, *ACS Appl. Mater. Interfaces*, 2014, **6**, 1933–1943.
36 L. F. He, R. G. Ma, N. Du, J. G. Ren, T. L. Wong, Y. Y. Li and S. T. Lee, *J. Mater. Chem.*, 2012, **22**, 19061–19066.
37 Z. L. Xiong, Y. S. Yun and H. J. Jin, *Materials*, 2013, **6**, 1138–1158.
38 J. Y. Eom, H. S. Kwon, J. Liu and O. Zhou, *Carbon*, 2004, **42**, 2589–2596.
39 D. Eder and A. H. Windle, *Adv. Mater.*, 2008, **20**, 1787–1793.
40 V. Etacheri, Y. Kuo, A. V. D. Ven and B. M. Bartlett, *J. Mater. Chem. A*, 2013, **1**, 12028–12032.
41 V. Etacheri, J. E. Yourey and B. M. Bartlett, *ACS Nano*, 2014, **8**, 1491–1499.
42 P. G. Bruce, B. Scrosati and J.-M. Tarascon, *Angew. Chem., Int. Ed.*, 2008, **47**, 2930–2946.
43 C. X. Peng, B. D. Chen, Y. Qin, S. H. Yang, C. Z. Li, Y. H. Zuo, S. Y. Liu and J. H. Yang, *ACS Nano*, 2012, **6**, 1074–1081.
44 W. S. Hummers Jr and R. E. Offeman, *J. Am. Chem. Soc.*, 1958, **80**, 1339.
45 Y. Wang, Y. Li, L. Tang, J. Lu and J. Li, *Electrochem. Commun.*, 2009, **11**, 889–892.
46 X. Y. Zhang, H. P. Li, X. L. Cui and Y. H. Lin, *J. Mater. Chem.*, 2010, **20**, 2801–2806.
47 X. Xin, X. Zhou, J. Wu, X. Yao and Z. Liu, *ACS Nano*, 2012, **6**, 11035–11043.
48 J. S. Chen, H. Liu, S. Z. Qiao and X. W. Lou, *J. Mater. Chem.*, 2011, **21**, 5687–5692.
49 S. J. Gregg and K. S. W. Sing, *J. Electrochem. Soc.*, 1967, **114**(11), 279C.